NANO LETTERS Cite This: Nano Lett. 2019, 19, 1158−1165
Letter
pubs.acs.org/NanoLett

Broadband Generation of Photonic Spin-Controlled Arbitrary Accelerating Light Beams in the Visible

Qingbin Fan,[†,‡] Wenqi Zhu,[§,∥] Yuzhang Liang,[†,‡] Pengcheng Huo,[†,‡] Cheng Zhang,[§,∥] Amit Agrawal,[§,∥] Kun Huang,[⊥] Xiangang Luo,[#] Yanqing Lu,[†,‡] Chengwei Qiu,[*,∇] Henri J. Lezec,[*,§] and Ting Xu[*,†,‡]

[†] National Laboratory of Solid State Microstructures, College of Engineering and Applied Sciences and Collaborative Innovation Center of Advanced Microstructures, Nanjing University, Nanjing 210093, China

[‡] Key Laboratory of Intelligent Optical Sensing and Manipulation, Ministry of Education, Nanjing 210093, China

[§] Center for Nanoscale Science and Technology, National Institute of Standards and Technology, Gaithersburg, Maryland 20899, United States

[∥] Maryland NanoCenter, University of Maryland, College Park, Maryland 20742, United States

[⊥] University of Science and Technology of China, Hefei 230026, China

[#] Institute of Optics and Electronics, Chinese Academy of Sciences, Chengdu 610209, China

[∇] Department of Electrical and Computer Engineering, National University of Singapore, 117583, Singapore

Supporting Information

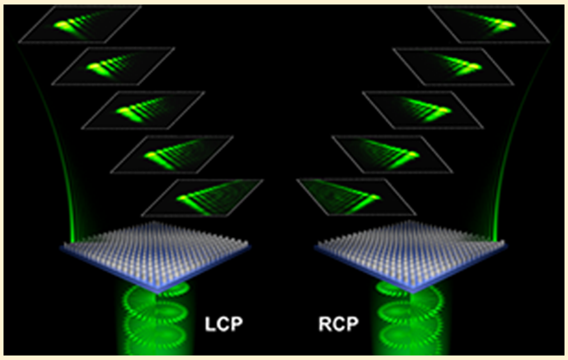

ABSTRACT: Bending light along arbitrary curvatures is a captivating and popular notion, triggering unprecedented endeavors in achieving diffraction-free propagation along a curved path in free-space. Much effort has been devoted to achieving this goal in homogeneous space, which solely relies on the transverse acceleration of beam centroid exerted by a beam generator. Here, based on an all-dielectric metasurface, we experimentally report a synthetic strategy of encoding and multiplexing acceleration features on a freely propagating light beam, synergized with photonic spin states of light. Independent switching between two arbitrary visible accelerating light beams with distinct acceleration directions and caustic trajectories is achieved. This proof-of-concept recipe demonstrates the strength of the designed metasurface chip: subwavelength pixel size, independent control over light beam curvature, broadband operation in the visible, and ultrathin scalable planar architecture. Our results open up the possibility of creating ultracompact, high-pixel density, and flat-profile nanophotonic platforms for efficient generation and dynamical control of structured light beams.

KEYWORDS: *Metasurface, accelerating light beams, nanostructures, visible wavelength*

Bending light beams along arbitrary curvatures could enable many intriguing phenomena and applications, such as optical illusion and cloaking.[1−4] However, generating curved light beams usually requires a background medium with gradient refractive index.[5−8] The curved trajectory typically expires quickly in a homogeneous medium due to the absence of transverse acceleration of the beam centroid. One solution entails imprinting incident light beam with a nonlinearly distributed phase profile to realize accelerating light beams (ALBs). As a fascinating caustic wave phenomenon, ALBs do not diffract while propagating along curved trajectories. For example, optical Airy beams, one representative form of ALB, have shape-preserving nature and their peak intensity follows a continuous parabolic curve as they propagate in free-space.[9,10] Their spatial evolution can be simply described by the paraxial Helmholtz equation, which has mathematical equivalence to its counterpart Schrödinger equation within the framework of quantum mechanics.[11]

Since the first experimental demonstration of optical Airy beams,[10] there have been numerous investigations on generalized ALBs that propagate along arbitrary convex trajectories,[12] including equivalent demonstrations in other field of physics such as with acoustic beams,[13] electron beams,[14] or surface plasmon polaritons.[15−17] Thanks to their unique nondiffractive nature, ALBs are a subject of intense current interest and have potential for applications in high-resolution light-sheet microscopy,[18] optical manipulation of biological cells,[19] generation of light-induced curved plasma

Received: November 13, 2018
Revised: December 26, 2018
Published: December 31, 2018

DOI: 10.1021/acs.nanolett.8b04571
Nano Lett. 2019, 19, 1158−1165

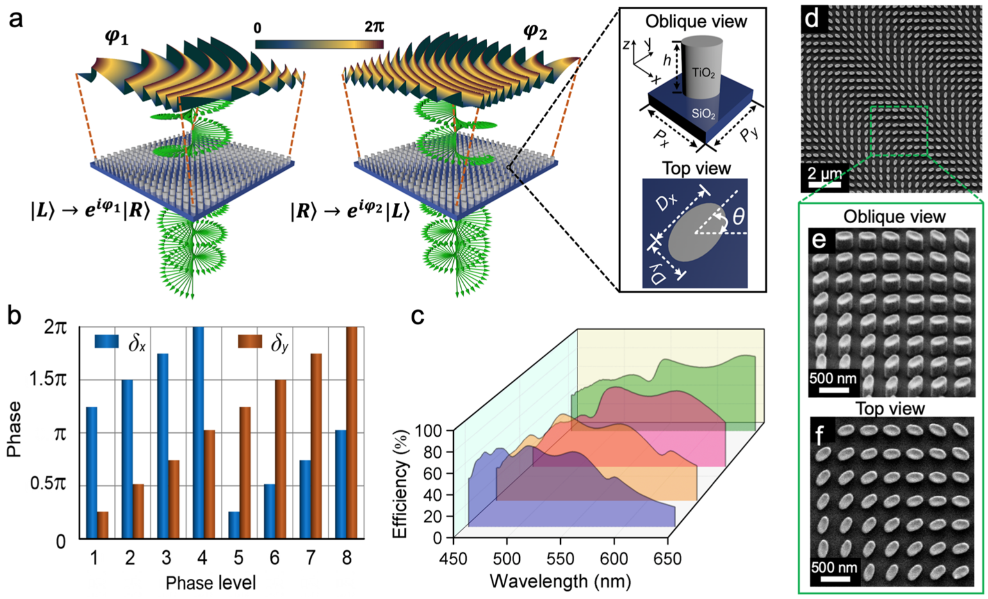

Figure 1. Photonic spin-controlled ALB metasurface generator. (a) Schematic diagram of the metasurface device capable of providing two independent phase profiles, φ_1 and φ_2, respectively for normally incident LCP and RCP light. Inset: perspective and top view of the metasurface unit cell formed by elliptical amorphous TiO_2 nanopost sitting on a silica substrate. (b) Calculated phase shifts, δ_x and δ_y, for different phase levels at a free-space wavelength of 532 nm. Each level corresponds to a specific TiO_2 nanopost birefringent wave-plate. (c) Calculated polarization conversion efficiencies of the chosen nanopost structures in the visible range. (d−f) SEM images of the fabricated metasurface device. The SEM image respectively show (d) a top view of large area, (e) zoomed view at an oblique angle, and (f) corresponding top view for the same area.

channels,[20] laser machining of curved microstructures,[21] and generation of light bullets.[22]

To date, most ALBs are generated by using a commercial spatial light modulator (SLM).[10,12,18−21,23−25] However, the large pixel size and pitch of SLMs inherently limit the available range of phase gradient and its accuracy. As a result, it is difficult to generate ALBs using SLMs with both fine spatial resolution and high precision. Moreover, the bulky footprint and high cost of SLMs pose a challenge for their integration within a compact nanophotonic platform. Although recently there have been attempts of using plasmonic nanoantennas to generate ALBs and demonstrate synchrotron radiation,[26,27] high intrinsic loss from metallic structures significantly limits beam generation efficiency. On the other hand, the ability to control and multiplex propagation characteristics of an ALB, such as its acceleration direction and caustic trajectory, has long been a challenge. Some progress has been made toward achieving dynamical control of the propagation trajectory of an ALB using second harmonic generation or three wave mixing in a nonlinear media.[28,29] Recent, acceleration control of Airy beams in a photorefractive crystal by applying ultrahigh voltages has been reported.[30] However, these schemes still have some limitations, either only work at specific frequencies and impose a stringent requirement on the ALB generation process or the acceleration control only can be realized inside the crystal but not in free-space. Hence, there is a need for realizing efficient generation mechanisms and arbitrary conversion platforms for ALBs that offer subwavelength pixel sizes, compact footprint, low cost, and broadband operation.

In this paper, we experimentally realize an ultrathin all-dielectric optical device to circumvent the aforementioned limitations and provide an efficient platform for both the generation and control of ALBs. In synergy with the photonic spin states of incident light, distinctively generated ALBs can propagate along arbitrary convex trajectories. We implement the strategy by using metasurfaces, which are arrays of planar subwavelength metallic or dielectric nanostructures.[31−54] Such two-dimensional metamaterials can alleviate some challenges of bulk metamaterials, including offering straightforward device fabrication, reducing volumetric losses and allowing compatibility with other on-chip photonic devices. In recent years, compared with metallic metasurfaces, all-dielectric metasurfaces have gained significant attention due to their capability of fully controlling wave-font of light with extremely low losses.[38−54] For dielectric metasufaces, the wavefront engineering of light typically relies on the modulation effect of either waveguide phase or geometric phase (or Pancharatnam-Berry phase), which can be realized by designing the nanostructures' lateral dimension and orientation angle of major axis relative to the reference coordinate, respectively. For example, visible light imaging has been demonstrated using a dielectric planar planar metalens exploiting rotated nanofin structures for nonresonant manipulation of geometric phase.[47] Other works, such as high-efficiency planar wave-plates,[48] Pancharatnam-Berry phase holography[49] and autofocusing vortical Airy beam generators[50] have also been proposed and experimentally or numerically demonstrated. In this work, we combine the modulation of both geometric phase and waveguide (or propagation) phase[53] to design a set of elliptical nanopost structures with different lateral sizes and orientation angles, to form the photonic-spin controlled metasurface ALB generators. The designed metasurface can provide two spin-dependent, fully uncorrelated arbitrary phase profiles for incident light with high transmission efficiency. This differs from the geometric phase-only modulation approach in which the generated spin-dependent phase profiles are correlative.[33,39,47] For experimental proof-of-concept, based on the paraxial caustic trajectory approach,[12] two dielectric metasurface devices operating at visible frequencies are designed and fabricated, exhibiting efficient generation of optical Airy beams

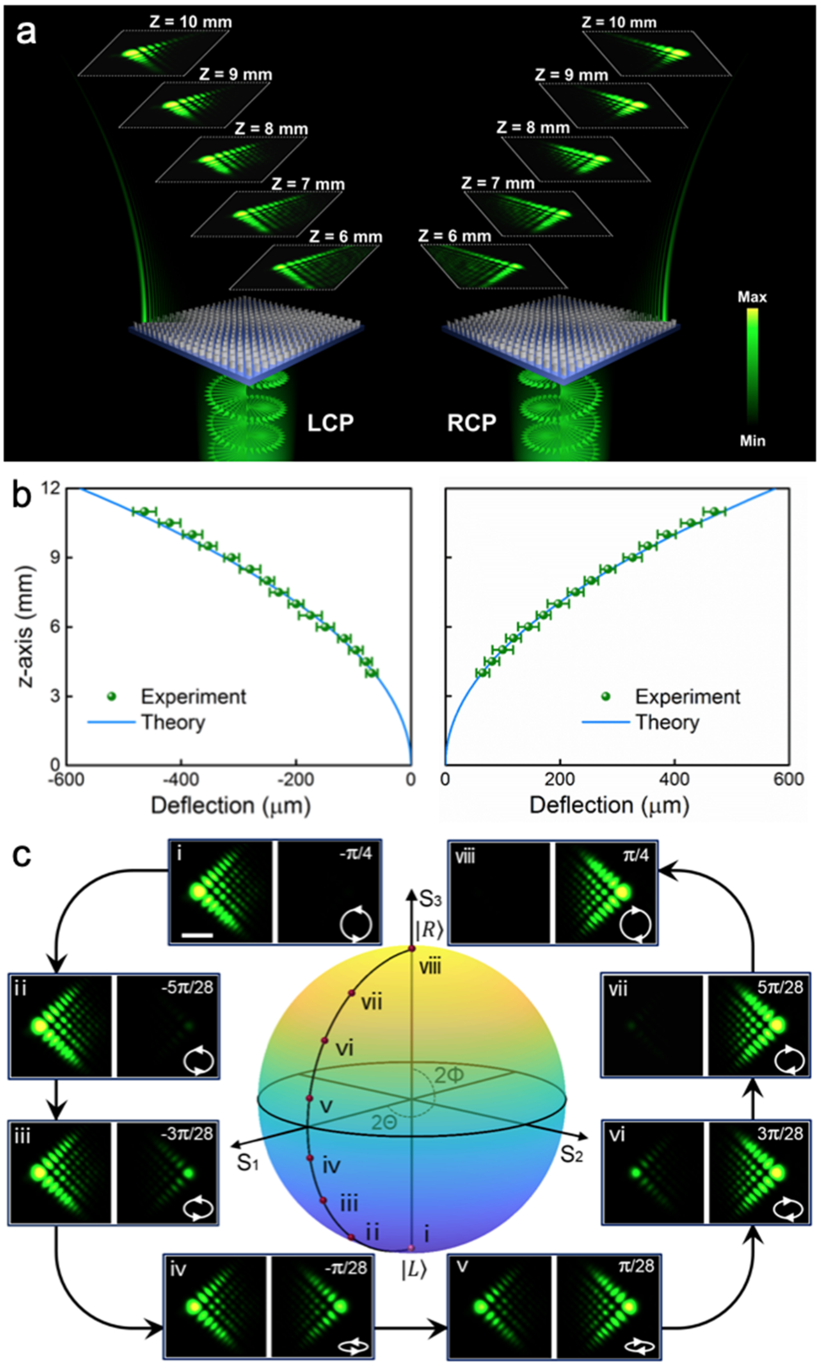

Figure 2. Generation of switchable optical Airy beams with opposite acceleration directions. (a) Schematic diagram of the experimental generation of optical Airy beams by the metasurface. The images in the white dashed frame show measured output intensities in the x–y plane along propagation trajectories for the incident light in LCP (left) and RCP (right). The wavelength of the incident light is 532 nm. (b) Experimentally measured (sphere) and theoretically calculated (solid line) Airy beams' propagation trajectories. The uncertainties are standard deviation of deflection distance for repeated experimental measurements (four in total). (c) Evolution of the output beams versus incident spin states. All the intensity profiles are taken at $z = 8$ mm. The circles with arrows on the Poincaré sphere show eight experimental incident spin states corresponding to intensity profiles i–viii. Scale bar for all the optical intensity images in (c), 50 μm.

with switchable opposite acceleration directions, and dynamic ALBs interchangeable between a natural logarithmic and biquadratic caustic trajectory. The spin state of incident light plays a coordinated role with two uncorrelated, polarization-dependent nonlinear phase profile of the dielectric metasurface to generate the requisite ALBs. We envision this work would inspire the creation of ultracompact flat-profile nanophotonic platforms for efficient generation and control of accelerating light beams and further promote their biomedical applications, such as integrated with endoscope[54] for high-resolution and large field-of-view bioimaging and dynamical cell manipulation.

Theory and Design. Figure 1a depicts an artistic rendering of the metasurface, consisting of an array of subwavelength elliptical dielectric nanoposts. The normally incident light onto the metasurface is assumed to be in two orthogonal spin states: $|L\rangle = \begin{bmatrix}1\\ i\end{bmatrix}$ and $|R\rangle = \begin{bmatrix}1\\ -i\end{bmatrix}$, where $|L\rangle$ and $|R\rangle$ denote left-circularly polarized (LCP) and right-circularly polarized (RCP) states, respectively. To generate two switchable accelerating beams (ALB_1 and ALB_2), the metasurface is required to provide two uncorrelated phase profiles $\varphi_1(x,y)$ and $\varphi_2(x,y)$ corresponding to the incident LCP and RCP spin states, respectively. Hence the metasurface can be described by a Jones matrix $J(x,y)$ which simultaneously satisfies $J(x,y)\,|L\rangle = e^{i\varphi_1(x,y)}|R\rangle$ and $J(x,y)\,|R\rangle = e^{i\varphi_2(x,y)}|L\rangle$.[51,52] That is, the input state $|L\rangle$ is interacting with the metasurface imparted the required phase factor $e^{i\varphi_1(x,y)}$ for ALB_1 while the input state $|R\rangle$ can be imparted the phase factor $e^{i\varphi_2(x,y)}$ for ALB_2, following the flipped handedness. Therefore, the Jones matrix $J(x,y)$ takes the form

$$J(x,\,y) = \frac{1}{2}\begin{bmatrix} e^{i\varphi_1(x,y)} + e^{i\varphi_2(x,y)} & ie^{i\varphi_2(x,y)} - ie^{i\varphi_1(x,y)} \\ ie^{i\varphi_2(x,y)} - ie^{i\varphi_1(x,y)} & -e^{i\varphi_1(x,y)} - e^{i\varphi_2(x,y)} \end{bmatrix} \tag{1}$$

On the basis of the eigenvalues and eigenvectors of the Jones matrix in eq 1, analytical solutions can be obtained for the required orientation angle for each constituent nanopost of the metasurface in the $x-y$ plane, $\theta(x,y)$, relative to the reference coordinate as $\theta(x,y) = [\varphi_1(x,y) - \varphi_2(x,y)]/4$. This orientation angle $\theta(x,y)$ determines the geometric phase imposed on the transmitted light. The corresponding phase shifts along the elliptical nanoposts' two perpendicular symmetry axes can then be expressed as $\delta_x(x,y) = [\varphi_1(x,y) + \varphi_2(x,y)]/2$ and $\delta_y(x,y) = \{[\varphi_1(x,y) + \varphi_2(x,y)]/2\} - \pi$, respectively (detailed calculations are shown in the Supporting Information Section S1). Therefore, it is imperative to find a set of nanoposts with phase shifts δ_x and δ_y covering an entire 2π phase range meanwhile satisfying $(\delta_x - \delta_y) = \pi$.

Inset of Figure 1a shows the artistic rendering of an individual unit cell of the designed metasurface, composed of an elliptical titanium dioxide (TiO_2) nanopost on a fused-silica substrate. We choose TiO_2 as the constituent material because of its large index of refraction and low loss at visible frequencies.[47,49,55] The TiO_2 elliptical nanoposts are designed to have identical heights of 600 nm but differ in their lateral dimensions D_x and D_y. This is used to control the waveguide phase, which is accumulated via the propagation of light inside the waveguide nanostructures and can be modulated by adjusting the lateral size of structures.[53] According to the calculated phase shifts and intensity transmission coefficients of x- and y-polarized light for TiO_2 elliptical nanoposts at a free-space wavelength of 532 nm (Supporting Information Figure S1), a set of eight nanostructures, including four fundamental nanoposts with different width (D_x, D_y) and their mirror structures with width (D_y, D_x), is designed which provide eight phase levels covering the 2π phase range for δ_x and δ_y, as shown in Figure 1b. These structural parameters are optimized such that the nanoposts' polarization conversion efficiencies are relatively high across the visible range (Figure 1c), which is a prerequisite for efficient broadband generation of ALBs (details about the definition of polarization conversion efficiencies are given in Supporting Information Section S2). All nanoposts are organized in a square array with a lattice constant of $P_x = P_y = 450$ nm along the x- and y-directions, respectively. As a result, the pixel area is more than 3 orders of magnitude smaller than the current commercial transmissive SLMs for the visible light (e.g., Holoeye LC2012 Transmissive SLM: 36 μm × 36 μm).[56] Thanks to its high refractive index, optical fields are mainly confined within individual TiO_2 nanoposts, and hence each nanopost can be regarded as an independent stand-alone cylindrical waveguide (Supporting Information Figure S2). Figure 1d−f shows the top-view and perspective-view scanning electron microscope (SEM) images of the fabricated TiO_2 metasurface. The complete fabrication process is described in the methods section.

Switchable Acceleration Directions of Optical Airy Beams. We first demonstrate a metasurface device capable of generating and switching the acceleration direction of optical Airy beam. The mapping between the incident and transmitted light through the metasurface follows $|L\rangle \rightarrow |R\rangle\,|A_l\rangle$ and $|R\rangle \rightarrow |L\rangle\,|A_r\rangle$, where $|A_l\rangle$ ($|A_r\rangle$) represents the state of Airy beam accelerating toward the left (right). According to the geometrical properties of optical caustics, ALBs along arbitrary convex trajectories can be generated by direct application of a spatial phase profile on an incident beam.[12] Here, we impose a 3/2 spatial phase function on an incident plane wave to obtain the required phase profile of the metasurface, and generate a two-dimensional Airy beam,[57,58] expressed as

$$\varphi_1(x,\,y) = -\frac{4}{3}n^{1/2}k(x^{3/2} + y^{3/2}) \tag{2}$$

where n is the acceleration coefficient associated with the contour of the Airy beam (here, $n = 4\ \text{m}^{-1}$ in metric units), $k = 2\pi/\lambda_0$ is the free-space wavevector and λ_0 is the free-space wavelength of operation ($\lambda_0 = 532$ nm). The parabolic caustic trajectory of the Airy beam can be expressed as a form of space curve: $\begin{cases} x = nz^2 \\ y = nz^2 \end{cases}$. The phase profile to generate an Airy beam with opposite acceleration direction can be obtained by $\varphi_2(x,y) = \varphi_1(w-x,w-y)$, where w is the side length of the square sample ensuring that the output positions of the two Airy beams are centrosymmetric.

The designed metasurface composed of TiO_2 nanopost array is fabricated with a lateral footprint of 540 μm × 540 μm on a fused-silica substrate. To characterize its performance, a normally incident collimated circularly polarized laser beam at a free-space wavelength of 532 nm is directed upon the metasurface from the substrate side. A schematic diagram of the measurement setup is shown in Supporting Information Figure S3. The parabolic trajectories of generated accelerating light beam are recorded by mapping the transverse intensity profiles of the transmitted light beam with a charge-coupled device (CCD) camera at different $x-y$ planes on the exit side of the metasurface ($z > 0$, Figure 2a). Under LCP illumination, the metasurface generates an Airy beam with a parabolic trajectory exhibiting a transverse acceleration toward the left side. The main lobe of the Airy beam maintains a spot size about 30 μm up to a propagation distance of 10 mm, clearly demonstrating the diffraction-free nature of an ALB propagating along a curved trajectory. As expected, when the spin state of the incident light is switched from LCP to RCP, a mirrored Airy beam with similar propagation trajectory but opposite acceleration direction is observed. The propagation characteristics and trajectories for both the left- and right-propagating Airy beams match well with the theoretical predictions (shown in Figure 2b). The experimentally measured Airy beam generation efficiency of the metasurface, defined as the ratio of the optical intensity of the generated ALB to the optical intensity of the incident light beam, is about 56%.

Figure 2c depicts the continuous evolution of the transverse light field at a distance of $z = 8$ mm from the exit surface of the metasurface ($z = 0$ mm) as the spin state of incident light is

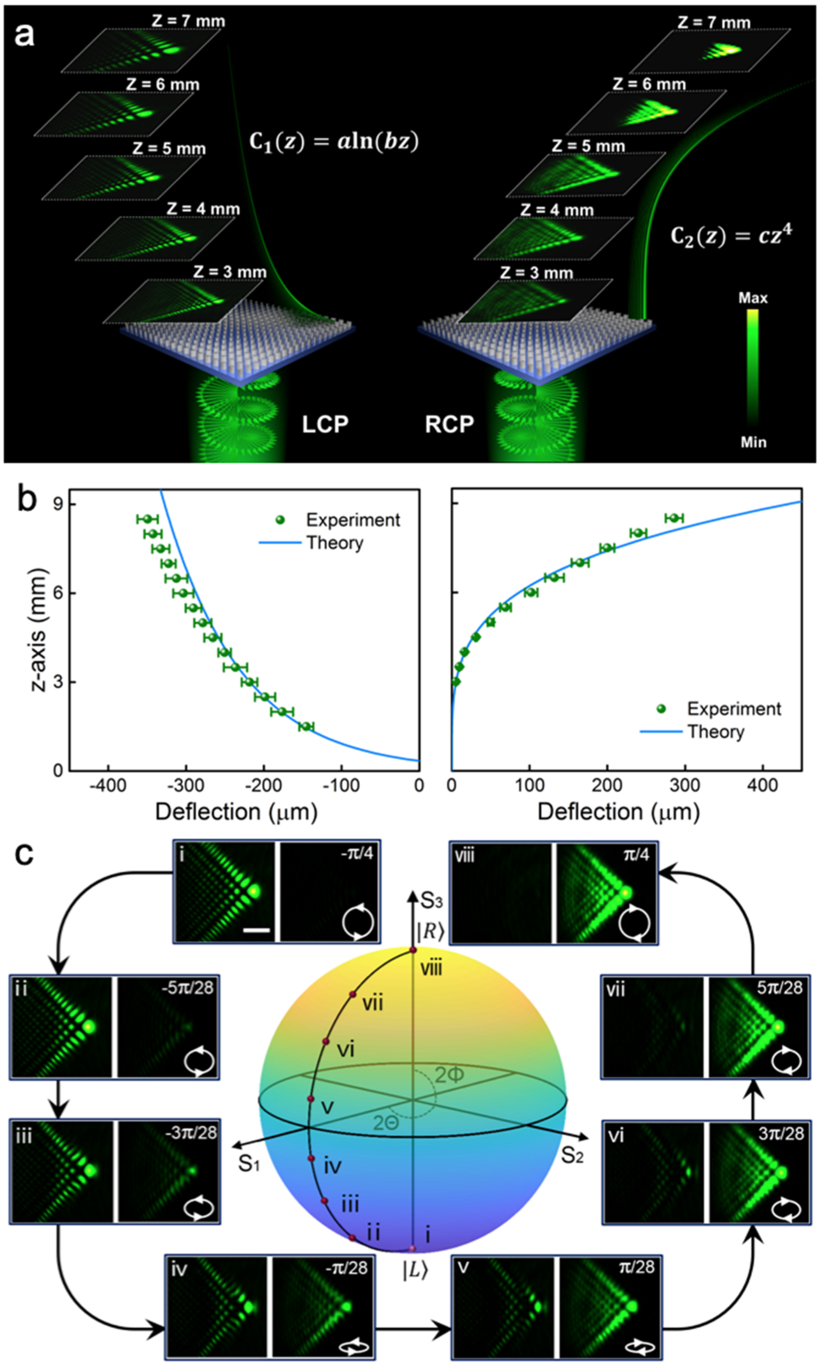

Figure 3. Generation of switchable ALBs along different caustic trajectories. (a) Schematic diagram of the experimental generation of ALBs respectively following natural logarithm and biquadratic caustic trajectories by metasurface. The images in the white dashed frame show measured output intensities in the x−y plane along propagation trajectories for the incident light with LCP (left) and RCP (right). (b) Experimentally measured (sphere) and theoretically calculated (solid line) two ALBs' propagation trajectories for LCP and RCP light. The uncertainties are standard deviation of deflection distance for repeated experimental measurements (four in total). (c) Evolution of the output beams versus incident spin states. All the intensity profiles are taken at z = 5 mm. The circles with arrows on the Poincaré sphere show eight experimental incident spin states corresponding to intensity profiles i−viii. Scale bar for all the intensity images in (c), 50 μm.

gradually modified from LCP to RCP using a quarter wave plate (QWP) with a rotation angle α relative to its fast axis increasing from $-\pi/4$ to $+\pi/4$. Because the input light with an arbitrary elliptical spin state on the Poincaré sphere is the superposition of two orthogonal spins $|L\rangle$ and $|R\rangle$, the two output states from the metasurface can be expressed as

$$|\Psi_l(\alpha)\rangle = \cos\left(\alpha + \frac{\pi}{4}\right)\cdot e^{-i(\alpha+\frac{\pi}{4})}|L\rangle|A_r\rangle \tag{3}$$

$$|\Psi_r(\alpha)\rangle = \sin\left(\alpha + \frac{\pi}{4}\right)\cdot e^{i(\alpha-\frac{\pi}{4})}|R\rangle|A_l\rangle \tag{4}$$

The optical intensity ratio K between these two states can be expressed as $K(\alpha) = \tan^2\left(\alpha + \frac{\pi}{4}\right)$. We extract the exper-

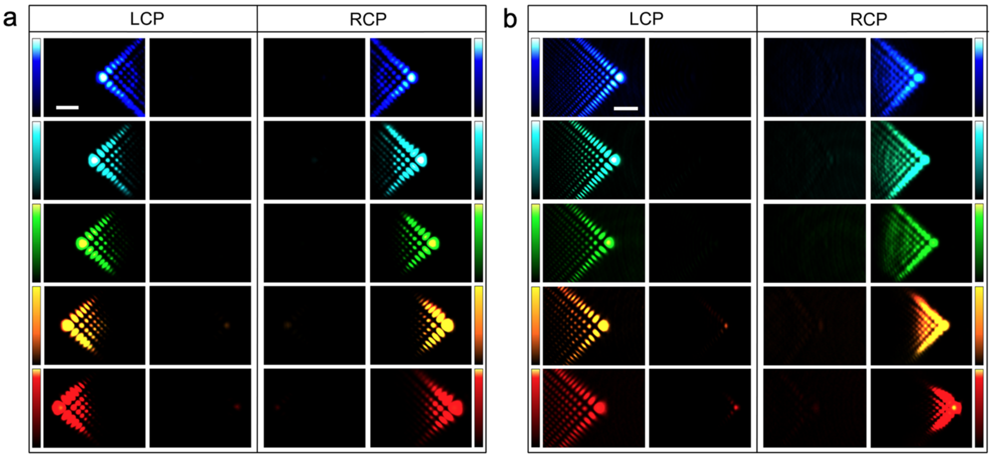

Figure 4. Broadband generation and control of ALBs. Experimentally measured intensity profiles of the generated (a) optical Airy beams (z = 8 mm) and (b) generalized acceleration light beams (z = 5 mm) by the two designed metasurface devices at free-space wavelengths of λ_0 = 460, 490, 532, 580, 610 nm. Scale bar for all the intensity images, 50 μm.

imentally measured intensity ratio K for the two opposite Airy beams as a function of α (Supporting Information Figure S4), and find it to be in good agreement with the theoretically predicted values. These results indicate that the intensities of the two generated Airy beams can be tuned by simply changing the spin state of incident light, making it beneficial for the trapping and release of multiple objects during an in situ optical manipulation experiment.

Arbitrary Caustic Trajectory Control of Accelerating Light Beams. In addition to controlling the acceleration direction, it is possible to achieve the generation and switching between two arbitrary ALBs that follow different caustic trajectories in free-space. As a proof-of-concept, here we report for the first time, a metasurface design that generates two output ALBs, one following a natural logarithmic and another a biquadratic caustic trajectory, expressed as space curve C_1, $\begin{cases} x = a\ln(bz) \\ y = a\ln(bz) \end{cases}$, and C_2, $\begin{cases} x = cz^4 \\ y = cz^4 \end{cases}$, respectively. The acceleration coefficients a, b, and c are freely used as arbitrarily chosen constants and here $a = -10^{-4}$ m, $b = 8 \times 10^3$ m^{-1}, and $c = 6.7 \times 10^4$ m^{-3} in metric units. The photonic spin-dependent phase profiles of the metasurface corresponding to LCP and RCP incident excitation are respectively expressed as

$$\varphi_1(x, y) = e^{-1}a^2bk[2 - exp^{(-x/a)} - exp^{(-y/a)}] \tag{5}$$

$$\varphi_2(x, y) = -\frac{16}{21}(3c)^{1/4}k(x^{7/4} + y^{7/4}) \tag{6}$$

Figure 3 shows the experimental results for this metasurface device illuminated with a normally incident circular polarized light at a free-space wavelength of 532 nm. Figure 3a shows the measured transverse field profiles of two-generated ALBs for various x−y planes at different z-positions on the exit-side of the metasurface ($z > 0$). Two-dimensional nondiffracting fields are measured along with their evolution dynamics. When illuminated with a LCP incident light, the accelerating beam generated by the metasurface follows the predesigned natural logarithm trajectory. When the incident light is switched to RCP, the generated beam propagates along a biquadratic curvature. In the latter case, the intensity cross-section of the beam becomes vague as the beam propagates farther away from the metasurface exit surface. This occurs because all the side lobes experience rapid deflection due to the biquadratic transverse acceleration and begin to converge with the main lobe.[12] Nevertheless, the propagation trajectories of these generated beams after passing through an ultrathin dielectric metasurface validate the theoretical predictions (Figure 3b). The experimentally measured generation efficiencies for ALBs following natural logarithm and biquadratic caustic trajectories are about 61% and 53%, respectively.

Figure 3c shows the continuous evolution of transverse intensity profile at a distance of z = 5 mm from the exit surface of the metasurface as the spin state of incident light is gradually changed from LCP to RCP. A gradual monotonic transition between the two distinct accelerating trajectories is clearly evident. Similar to the demonstration with Airy beams discussed above, the intensities of the two arbitrary ALBs can be tuned by changing the spin state along the Poincaré sphere. The theoretical and experimentally measured intensity ratio $K(\alpha)$ for the two ALBs as a function of rotation angle α of the QWP are discussed in Supporting Information Figure S4.

Broadband Operations of Accelerating Light Beams. Figure 4 shows the experimental results for the two metasurface devices, discussed in the previous sections, illuminated at five different free-space wavelengths across the visible region (λ_0 = 460, 490, 532, 580, 610 nm). It is clearly evident from the lateral intensity profiles that the transmitted beam still exhibits a two-dimensional Airy-like interference pattern except that the position of main lobe at each wavelength is shifted laterally. Although the metasurfaces can generate ALBs in the broad range of visible wavelengths, the trajectories of the generated ALBs are still wavelength-dependent due to chromatic diffraction dispersion. The corresponding propagation trajectories for the three types of ALBs are summarized in Supporting Information Figure S5−S7. In principle, a two-dimensional ALB can be treated as a superposition of two one-dimensional ALBs traveling along two orthogonal directions. Under the paraxial approximation, for a two-dimensional ALB with a caustic trajectory $C(z)$: $\begin{cases} x = g(z) \\ y = f(z) \end{cases}$, the required phase at the exit surface (z = 0) is given by[58]

$$\varphi(x, y) = k\left[\int g'(z)\mathrm{d}x + \int f'(z)\mathrm{d}y\right] \tag{7}$$

where $g(z)$ and $f(z)$ are two continuous functions and respectively indicate the projection of the caustic trajectory of two-dimensional ALB in x–z and y–z plane, and the superscript “′” denotes partial differentiation. As shown in Supporting Information Figure S8, the phase profiles $\varphi(x,y)$ of the TiO_2 metasurface are almost the same for the selected multiwavelengths. Therefore, based on eq 7, by increasing the free-space wavelength λ_0, $g'(z)$ and $f'(z)$ also increase, resulting in a larger deflection for the generated ALB. This prediction agrees well with the experimental observations shown in Figure 4 and Supporting Information Figure S5–S7. The experimentally measured generation efficiencies of the two metasurfaces for ALBs at different wavelengths range from 31% to 61% (Supporting Information Table S1).

Furthermore, as shown in Figure 4, the acceleration direction and caustic trajectories of the generated ALBs at these multiple incident wavelengths still depend on the spin states of incident light. This occurs because TiO_2 nanoposts have relatively high polarization conversion efficiencies at these wavelengths and can be treated as half-wave plates. As a result, they can generate geometrical phases for the incident light solely based on their rotation angle θ. These wavelength-insensitive geometrical phases are associated with the eigenvectors of the Jones matrix $J(x,y)$ of the metasurfaces, and enable the photonic spin-control functionality. Our results explicitly show that these metasurface devices can simultaneously achieve efficient and broadband generation and dynamic control of ALBs in the visible region, which are not readily achievable from conventional methods based on SLMs.

In conclusion, we have demonstrated an ultrathin all-dielectric metasurface device that can achieve robust generation and switch between two arbitrary accelerating light beams at multiple wavelength across the visible region. The propagation characteristics of the metasurface-assisted ALBs, including acceleration direction and caustic trajectory, can be well controlled and manipulated. Compared with previous demonstrations of ALB generation, the single layer and ultrathin architecture of the metasurfaces realized here enables a low-cost, scalable and integration friendly platform for structured light generation, and its applications.

Experimental Methods. *Sample Fabrication.* The 500 μm thick, double-side polished fused silica substrates were first prime-vapor-coated with a monolayer of hexamethyldisilazane (HMDS) and then spin-coated with a layer of 600 nm thick, ZEP520A positive-tone electron beam (e-beam) resist. Afterward, the samples were coated with a layer of 10 nm thick aluminum (Al) via thermal evaporation, which suppressed the charging effect during the subsequent e-beam lithography step. The e-beam lithography was performed at an accelerating voltage of 100 kV and beam current of 2 nA. The samples were developed in hexyl-acetate for 120 s. Next, the patterned samples were coated with TiO_2 using atomic layer deposition (ALD). The ALD was done at a low temperature of 90 °C to avoid deformation of the resist pattern. After the ALD, the overcoated TiO_2 layer was etched by the inductively coupled-plasma reactive ion etching (ICP-RIE), with a gas mixture of Cl_2 and BCl_3. The etching was stopped when the overcoated TiO_2 had been fully removed and the e-beam resist was exposed. Finally, the samples were exposed to UV irradiation, followed by soaking in *n*-methyl-2-pyrrolidone, which removed the resist and produced the array of TiO_2 nanoposts with predesigned geometries.

ASSOCIATED CONTENT

Supporting Information

The Supporting Information is available free of charge on the ACS Publications website at DOI: 10.1021/acs.nanolett.8b04571.

> Derivation of Jones matrix, calculation and simulation of phase modulation in dielectric nanoposts, illustration of the experimental setup, propagation trajectories of accelerating beams at different visible wavelengths, beam generation efficiencies of metasurface devices (PDF)

AUTHOR INFORMATION

Corresponding Authors

*E-mail: xuting@nju.edu.cn.
*E-mail: henri.lezec@nist.gov.
*E-mail: chengwei.qiu@nus.edu.sg.

ORCID

Cheng Zhang: 0000-0002-9739-3511
Xiangang Luo: 0000-0002-1401-1670
Ting Xu: 0000-0002-0704-1089

Author Contributions

Q.F., W.Z., and Y.L. contributed equally. All authors contributed to the interpretation of results and participated in manuscript preparation. T. X. directed the project.

Notes

The authors declare no competing financial interest.

ACKNOWLEDGMENTS

This work is supported in part by the National Key R&D Program of China under Grants 2017YFA0303700 and 2016YFA0202100, National Natural Science Foundation of China (61575092 and 11774163), Fundamental Research Funds for Central Universities under Grant 14380078. C.Z., W.Z., and A.A. acknowledge support under the Cooperative Research Agreement between the University of Maryland and the National Institute of Standards and Technology Center for Nanoscale Science and Technology, Award #70NANB14H209. C.W.Q. acknowledges the financial support from the National Research Foundation, Prime Minister's Office, Singapore under its Competitive Research Program (CRP award NRF CRP15-2015-03).

REFERENCES

(1) Cai, W.; Chettiar, U. K.; Kildishev, A. V.; Shalaev, V. M. *Nat. Photonics* **2007**, *1*, 224–227.

(2) Li, J.; Pendry, J. B. *Phys. Rev. Lett.* **2008**, *101*, 203901.

(3) Valentine, J.; Li, J.; Zentgraf, T.; Bartal, G.; Zhang, X. *Nat. Mater.* **2009**, *8*, 568–571.

(4) Gabrielli, L. H.; Cardenas, J.; Poitras, C. B.; Lipson, M. *Nat. Photonics* **2009**, *3*, 461–463.

(5) Pendry, J. B.; Schurig, D.; Smith, D. R. *Science* **2006**, *312*, 1780–1782.

(6) Leonhardt, U. *Science* **2006**, *312*, 1777–1780.

(7) Chen, H.; Chan, C. T.; Sheng, P. *Nat. Mater.* **2010**, *9*, 387–396.

(8) Sheng, C.; Liu, H.; Wang, Y.; Zhu, S. N.; Genov, D. A. *Nat. Photonics* **2013**, *7*, 902–906.

(9) Siviloglou, G. A.; Christodoulides, D. N. *Opt. Lett.* **2007**, *32*, 979–981.

(10) Siviloglou, G. A.; Broky, J.; Dogariu, A.; Christodoulides, D. N. *Phys. Rev. Lett.* **2007**, *99*, 213901.

(11) Berry, M. V.; Balazs, M. *Am. J. Phys.* **1979**, *47*, 264.

(12) Greenfield, E.; Segev, M.; Walasik, W.; Raz, O. *Phys. Rev. Lett.* **2011**, *106*, 213902.

(13) Zhang, P.; Li, T. C.; Zhu, J.; Zhu, X. F.; Yang, S.; Wang, Y.; Yin, X. B.; Zhang, X. *Nat. Commun.* **2014**, *5*, 4316.

(14) Voloch-Bloch, N.; Lereah, Y.; Lilach, Y.; Gover, A.; Arie, A. *Nature* **2013**, *494*, 331−335.

(15) Salandrino, A.; Christodoulides, D. N. *Opt. Lett.* **2010**, *35*, 2082.

(16) Minovich, A.; Klein, A. E.; Janunts, N.; Pertsch, T.; Neshev, D. N.; Kivshar, Y. S. *Phys. Rev. Lett.* **2011**, *107*, 116802.

(17) Li, L.; Li, T.; Wang, S. M.; Zhang, C.; Zhu, S. N. *Phys. Rev. Lett.* **2011**, *107*, 126804.

(18) Vettenburg, T.; Dalgarno, H. I. C.; Nylk, J.; Coll-Lladó, C.; Ferrier, D. E. K.; Čižmár, T.; Gunn-Moore, F. J.; Dholakia, K. *Nat. Methods* **2014**, *11*, 541−544.

(19) Dholakia, K.; Čižmár, T. *Nat. Photonics* **2011**, *5*, 335−342.

(20) Polynkin, P.; Kolesik, M.; Moloney, J. V.; Siviloglou, G. A.; Christodoulides, D. N. *Science* **2009**, *324*, 229−232.

(21) Mathis, A.; Courvoisier, F.; Froehly, L.; Furfaro, L.; Jacquot, M.; Lacourt, P. A.; Dudley, J. M. *Appl. Phys. Lett.* **2012**, *101*, 071110.

(22) Chong, A.; Renninger, W. H.; Christodoulides, D. N.; Wise, F. W. *Nat. Photonics* **2010**, *4*, 103−106.

(23) Siviloglou, G. A.; Broky, J.; Dogariu, A.; Christodoulides, D. N. *Opt. Lett.* **2008**, *33*, 207−209.

(24) Broky, J.; Siviloglou, G. A.; Dogariu, A.; Christodoulides, D. N. *Opt. Express* **2008**, *16*, 12880−12891.

(25) Papazoglou, D. G.; Efremidis, N. K.; Christodoulides, D. N.; Tzortzakis, S. *Opt. Lett.* **2011**, *36*, 1842−1844.

(26) Henstridge, M.; Pfeiffer, C.; Wang, D.; Boltasseva, A.; Shalaev, V. M.; Grbic, A.; Merlin, R. *Optica* **2018**, *5*, 678−681.

(27) Henstridge, M.; Pfeiffer, C.; Wang, D.; Boltasseva, A.; Shalaev, V. M.; Grbic, A.; Merlin, R. *Science* **2018**, *362*, 439−442.

(28) Ellenbogen, T.; Bloch, N. V.; Ganany-Padowicz, A.; Arie, A. *Nat. Photonics* **2009**, *3*, 395−398.

(29) Dolev, I.; Ellenbogen, T.; Arie, A. *Opt. Lett.* **2010**, *35*, 1581.

(30) Ye, Z.; Liu, S.; Lou, C.; Zhang, P.; Hu, Y.; Song, D.; Zhao, J.; Chen, Z. *Opt. Lett.* **2011**, *36*, 3230−3232.

(31) Yu, N.; Genevet, P.; Kats, M. A.; Aieta, F.; Tetienne, J. P.; Capasso, F.; Gaburro, Z. *Science* **2011**, *334*, 333−337.

(32) Ni, X.; Emani, N. K.; Kildishev, A. V.; Boltasseva, A.; Shalaev, V. M. *Science* **2012**, *335*, 427.

(33) Chen, X.; Huang, L.; Mühlenbernd, H.; Li, G.; Bai, B.; Tan, Q.; Jin, G.; Qiu, C.; Zhang, S.; Zentgraf, T. *Nat. Commun.* **2012**, *3*, 1198.

(34) Luo, X. *Sci. China: Phys., Mech. Astron.* **2015**, *58*, 594201.

(35) Tymchenko, M.; Gomez-Diaz, J. S.; Lee, J.; Nookala, N.; Belkin, M. A.; Alù, A. *Phys. Rev. Lett.* **2015**, *115*, 207403.

(36) Kuznetsov, A. I.; Miroshnichenko, A. E.; Brongersma, M. L.; Kivshar, Y. S.; Lukyanchuk, B. *Science* **2016**, *354*, aag2472.

(37) Ren, H.; Li, X.; Zhang, Q.; Gu, M. *Science* **2016**, *352*, 805−809.

(38) Lin, D.; Fan, P.; Hasman, E.; Brongersma, M. L. *Science* **2014**, *345*, 298−302.

(39) Khorasaninejad, M.; Crozier, K. B. *Nat. Commun.* **2014**, *5*, 5386.

(40) Arbabi, A.; Horie, Y.; Ball, A. J.; Bagheri, M.; Faraon, A. *Nat. Commun.* **2015**, *6*, 7069.

(41) Arbabi, A.; Horie, Y.; Bagheri, M.; Faraon, A. *Nat. Nanotechnol.* **2015**, *10*, 937−943.

(42) Arbabi, A.; Arbabi, E.; Kamali, S. M.; Horie, Y.; Han, S.; Faraon, A. *Nat. Commun.* **2016**, *7*, 13682.

(43) Arbabi, A.; Arbabi, E.; Horie, Y.; Kamali, S. M.; Faraon, A. *Nat. Photonics* **2017**, *11*, 415.

(44) Chen, W. T.; Zhu, A. Y.; Sanjeev, V.; Khorasaninejad, M.; Shi, Z.; Lee, E.; Capasso, F. *Nat. Nanotechnol.* **2018**, *13*, 220−226.

(45) Wang, S. M.; Wu, P. C.; Su, V. C.; Lai, Y. C.; Chen, M. K.; Kuo, H. Y.; Chen, B. H.; Chen, Y. H.; Huang, T. T.; Wang, J. H.; Lin, R. M.; Kuan, C. H.; Li, T.; Wang, Z. L.; Zhu, S. N.; Tsai, D. P. *Nat. Nanotechnol.* **2018**, *13*, 227−232.

(46) Jang, M.; Horie, Y.; Shibukawa, A.; Brake, J.; Liu, Y.; Kamali, S. M.; Arbiba, A.; Ruan, H. W.; Faraon, A.; Yang, C. *Nat. Photonics* **2018**, *12*, 84.

(47) Khorasaninejad, M.; Chen, W. T.; Devlin, R. C.; Oh, J.; Zhu, A. Y.; Capasso, F. *Science* **2016**, *352*, 1190−1194.

(48) Kruk, S.; Hopkins, B.; Kravchenko, I. I.; Miroshnichenko, A.; Neshev, D. N.; Kivshar, Y. *APL Photonics* **2016**, *1*, 030801.

(49) Devlin, R. C.; Khorasaninejad, M.; Chen, W. T.; Oh, J.; Capasso, F. *Proc. Natl. Acad. Sci. U. S. A.* **2016**, *113*, 10473−10478.

(50) Fan, Q.; Wang, D.; Huo, P.; Zhang, Z.; Liang, Y.; Xu, T. *Opt. Express* **2017**, *25*, 9285−9294.

(51) Mueller, J. P. B.; Rubin, N. A.; Devlin, R. C.; Groever, B.; Capasso, F. *Phys. Rev. Lett.* **2017**, *118*, 113901.

(52) Devlin, R. C.; Ambrosio, A.; Rubin, N. A.; Mueller, J. B.; Capasso, F. *Science* **2017**, *358*, 896−901.

(53) Chen, S.; Li, Z.; Zhang, Y.; Cheng, H.; Tian, J. *Adv. Opt. Mater.* **2018**, *6*, 1088104.

(54) Pahlevaninezhad, H.; Khorasaninejad, M.; Huang, Y. W.; Shi, Z.; Hariri, L. P.; Adams, D. C.; Ding, V.; Zhu, A.; Qiu, C. W.; Capasso, F.; Suter, M. J. *Nat. Photonics* **2018**, *12*, 540−547.

(55) Lalanne, P.; Astilean, S.; Chavel, P.; Cambril, E.; Launois, H. *Opt. Lett.* **1998**, *23*, 1081−1083.

(56) http://holoeye.com/spatial-light-modulators/ The identification of any commercial product or trade name is used to foster understanding. Such identification does not imply recommendation or endorsement or by the National Institute of Standards and Technology, nor does it imply that the materials or equipment identified are necessarily the best available for the purpose.

(57) Cottrell, D. M.; Davis, J. A.; Hazard, T. M. *Opt. Lett.* **2009**, *34*, 2634−2636.

(58) Froehly, L.; Courvoisier, F.; Mathis, A.; Jacquot, M.; Furfaro, L.; Giust, R.; Lacourt, P. A.; Dudley, J. M. *Opt. Express* **2011**, *19*, 16455−16465.